Journal of
METAMORPHIC GEOLOGY

J. metamorphic Geol., 2013, **31,** 131–146 doi:10.1111/jmg.12003

Staurolite porphyroblast controls on local bulk compositional and microstructural changes during decompression of a St–Bt–Grt–Crd–And schist (Ancasti metamorphic complex, Sierras Pampeanas, W Argentina)

S. O. VERDECCHIA,[1] J. RECHE,[2] E. G. BALDO,[1] E. SEGOVIA-DIAZ[3] AND F. J. MARTINEZ[2]
[1]*CICTERRA (CONICET-Universidad Nacional de Córdoba), Facultad de Ciencias Exactas, Físicas y Naturales. Av. Vélez Sarsfield 1611, X5016CGA Córdoba, Argentina (sverdecchia@gmail.com; sverdecchia@efn.uncor.edu)*
[2]*Departament de Geologia, Universitat Autónoma de Barcelona, 08193 Bellaterra, Spain*
[3]*Dpto. de Petrología y Geoquímica, CSIC-Universidad Complutense, 28040 Madrid, Spain*

ABSTRACT The staurolite–biotite–garnet–cordierite–andalusite–plagioclase–muscovite–quartz metapelitic mineral assemblage has been frequently interpreted in the literature as a result of superimposition of various metamorphic events, for example, in polymetamorphic sequences. The assemblage was identified in schists from the Ancasti metamorphic complex (Sierras Pampeanas of Argentina) where previous authors have favoured the polymetamorphic genetic interpretation. A pseudosection in the MnNCKFMASH system for the analysed XRF bulk composition predicts the stability of the sub-assemblage staurolite–biotite–garnet–plagioclase–muscovite–quartz, and the compositional isopleths also agree with measured mineral compositions. Nevertheless, the XRF pseudosection does not predict any field with staurolite, andalusite and cordierite being stable together. As a result of more detailed modelling making use of the effective bulk composition concept, our interpretation is that the staurolite–biotite–garnet–plagioclase–muscovite–quartz sub-assemblage was present at peak metamorphic conditions, 590 °C and 5.2 kbar, but that andalusite and cordierite grew later along a continuous *P–T* path. These minerals are not in mutual contact and are observed in separate microstructural domains with different proportions of staurolite. These domains are explained as a result of local reaction equilibrium subsystems developed during decompression and influenced by the previous peak crystal size and local modal distribution of staurolite porphyroblasts that have remained metastable. Thus, andalusite and cordierite grew synchronously, although in separate microdomains, and represent the decompression stage at 565 °C and 3.5 kbar.

Key words: effective bulk composition; microstructure; MnNCKFMASH; pseudosections; retrogression.

INTRODUCTION

Geothermobarometric calculations applied to metamorphic assemblages have undergone a change of course in the last 20 years with the development of the equilibrium thermodynamics mineral modelling approach that uses *P–T*, *P–X* and *T–X* pseudosection diagrams derived from treatment of internally consistent thermodynamic data sets (e.g. see Powell & Holland, 2008) with specific computer programs as THERMOCALC (Powell & Holland, 1988) or PERPLE_X (Connolly, 1990). The pseudosection diagrams display predicted stable mineral assemblages in a range of *P–T* conditions for a given specific bulk composition. Continuous and discontinuous changes in mineral mode and composition can also be represented (see Powell *et al.*, 1998) through modal and compositional isopleths drawn on such diagrams. The applicability of this approach depends on many factors, such as the appropriate selection of the chemical system (bulk composition) and the quality of the mineral solution models (see Powell & Holland, 2008). It has been realized that during prograde and/or retrograde *P–T* paths, reacting metamorphic systems can undergo domain chemical fractionations that depend on a variety of factors, such as microstructural changes including evolving grain size or changes in diffusion properties causing cores of zoned porphyroblasts to be isolated from the reacting system (e.g. Evans, 2004; Jeřábek *et al.*, 2008). Thus, the instantaneous reacting bulk composition or effective bulk composition (EBC) can change along the *P–T* path (Stüwe, 1997). These processes are important during cooling due to progressively slower diffusion rates that limit elemental exchange and net transfer. Thus, it has become increasingly evident that interpreting a full prograde–retrograde *P–T* path using a unique pseudosection must be incorrect, as significant changes of equilibrium

volume and equilibrium bulk composition are not usually considered at all. Among the factors that can influence the genesis of such equilibrium volumes and its particular evolution during a *P–T* path, this paper has focused on the heterogeneous distribution and size of porphyroblasts.

The staurolite–biotite–garnet–cordierite–andalusite assemblage was identified in metapelitic schists from the Ancasti metamorphic complex (Sierras Pampeanas, Argentina) where it is characterized by the presence of large staurolite porphyroblasts. This assemblage is generally regarded as not being in full equilibrium and has often been ascribed to a polymetamorphic history (Pattison *et al.*, 1999; Tinkham *et al.*, 2001). In other cases, staurolite has been considered to have remained as a metastable phase inside the andalusite stability field although still pertaining to a single, continuous metamorphic event (García-Casco & Torres-Roldán, 1999; Ali, 2010). In the present work, the term 'metamorphic event' is applied in the sense described by Vernon *et al.* (2008); that is a distinct tectonothermal episode composed of prograde, peak and retrograde stages, which can encompass several deformation episodes.

The main goal of this research is to analyse the stability of the staurolite–biotite–garnet–cordierite–andalusite assemblage from the Ancasti metamorphic complex and to determine the influence of peak microstructural features, such as staurolite porphyroblast size and distribution, on successive changes in EBC and mineral stability during post-peak evolution. Therefore, the identification of mineral assemblages containing metastable phases and segregation of EBC domains along *P–T* paths are critical factors in the correct interpretation and discrimination between single metamorphic and polymetamorphic events.

THE ANCASTI METAMORPHIC COMPLEX

The Ancasti metamorphic complex (Knüver & Miller, 1981; Miró *et al.*, 2004) in the Sierra de Ancasti, Eastern Sierras Pampeanas (central west of Argentina, Fig. 1a), is one of the complexes associated with the Early Palaeozoic evolution of southwestern Proto-Andean margin of Gondwana (e.g. Pankhurst & Rapela, 1998; Rapela *et al.*, 2005). This complex is composed of a several-kilometre thick early Palaeozoic metasedimentary sequence that can be divided into three main segments (Fig. 1b): (i) quartz–mica schists, quartzites, biotite-bearing paragneisses, pure and calc–silicate marbles and metabasites in the eastern flank, (ii) banded schists (rhythmic intercalation of millimetre quartz-rich and mica-rich layers; Fig. 1c), quartz–biotitic schists and calc–silicates in the central region, and (iii) migmatites and paragneisses in the western flank (Willner *et al.*, 1983; Rapela *et al.*, 2005). This sequence underwent regional folding, with NNW–SSE tight folds and large-scale flexures (Willner, 1983a). A Late Neoproterozoic sedimentary maximum age for the banded schist unit was determined on the basis of U-Pb SHRIMP zircon ages (youngest age peak at *c.* 570 Ma; Rapela *et al.*, 2007), whereas an Ediacaran depositional age of 590–570 Ma was inferred for the marbles by reference to the trend of $^{87}Sr/^{86}Sr$ in Neoproterozoic seawater (Murra *et al.*, 2011). This complex was intruded by kilometre-sized Ordovician and Carboniferous granitic and granodioritic plutons (Knüver, 1983; Rapela *et al.*, 2005; Dahlquist *et al.*, 2012; Fig. 1b). Pegmatitic bodies occur in a narrow belt near the sillimanite–K-feldspar isograd (western sector of the Sierra de Ancasti; see Lottner, 1983).

This metasedimentary succession records a complex tectonothermal history as shown by Willner (1983a,b). This author proposed: (i) a poorly preserved early S_1 compositional banding (D_1 episode) coeval with a low-grade metamorphism (M_1); (ii) a S_2 pressure solution compositional banding (D_2 episode) linked to strong regional isoclinal folding developed under low-grade metamorphic conditions (M_2); (iii) a D_3 folding episode (S_3 foliation) followed by a post-tectonic thermal event of low to intermediate pressure (M_3) responsible for the regional metamorphic zoning whose grade increases from east to west from almandine, through staurolite–cordierite–andalusite, to cordierite–sillimanite–K-feldspar zones; and (iv) a weak D_4 folding (S_4) episode related to retrograde mineral growth (chlorite and muscovite; M_4 metamorphic event). Moreover, Baldo *et al.* (2008) recognized primary cross-bedding sedimentary structures in the banded schist and reinterpreted the compositional banding, represented by S_1 and S_2, as relict stratification ($S_0 + S_1$, Fig. 1c). Knüver (1983) determined a Cambrian age (*c.* 530 Ma) for the low-grade metamorphic event (M_2) and an Ordovician age for M_3 (*c.* 472 Ma) using whole-rock Rb–Sr dating.

Staurolite–biotite–garnet–cordierite–andalusite–quartz–muscovite schists

The staurolite–biotite–garnet–cordierite–andalusite–plagioclase–muscovite–quartz assemblage occurs in centimetre- to metre-thick quartz–mica schist layers of the staurolite–cordierite–andalusite zone intercalated within the banded schist unit in the central segment of the Ancasti metamorphic complex (Baldo *et al.*, 2008; Fig. 1d). In this study, a representative sample of this banded schist unit (ANC-19000) was collected from the central sector, SE of Yerba Buena town (29°01′18.80″S 65°26′1.30″W; Fig. 1b).

PETROGRAPHY AND MICROSTRUCTURAL RELATIONSHIPS

The studied sample (ANC-19000) of quartz–mica schist contains staurolite, cordierite, andalusite, garnet, biotite, muscovite, quartz, plagioclase, chlorite plus accessories (ilmenite, zircon, monazite, tourmaline, apatite, magnetite and rutile). This sample shows a heterogeneous min-

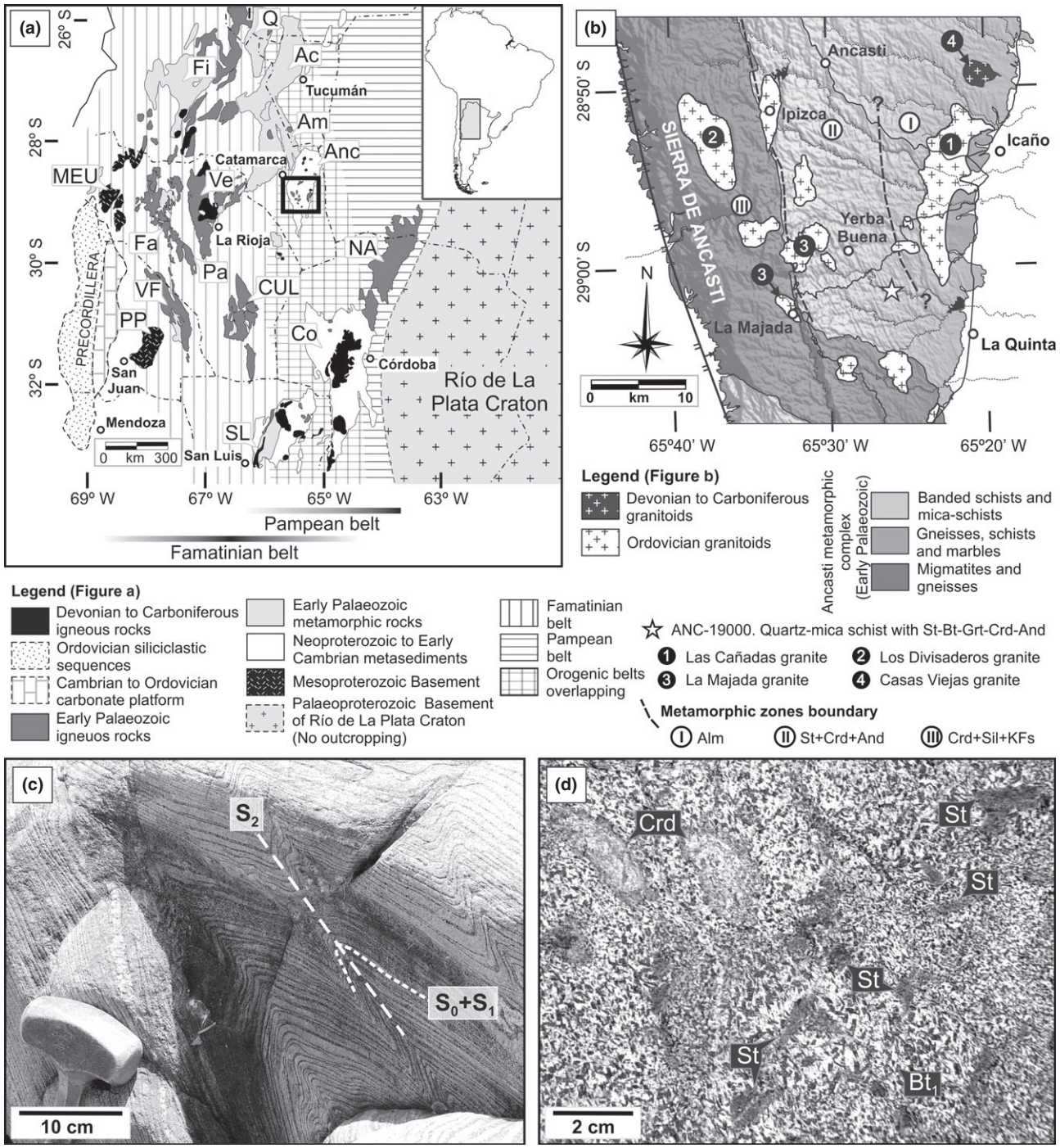

Fig. 1. (a) Sketch map of central west Argentina showing the Sierras Pampeanas and Precordillera regions and the extent of orogenic belts. (b) Geological map of central region of the Sierra de Ancasti (Catamarca province) showing the main lithologies of the Ancasti metamorphic complex (after Murra *et al.*, 2011). The boundary of the N–S extended zone is not still well known. (c) Folding of the layering of the Ancasti banded schist. (d) Details of a metapelitic layer with staurolite, biotite, cordierite, andalusite and garnet porphyroblasts. Abbreviation of main Sierras: Quilmes (Q), Fiambala (Fi), Aconquija (Ac), Ambato (Am), Ancasti (Anc), Velasco (Ve), Maz–Espinal–Umango (MEU), Famatina (Fa), Paganzo (Pa), Norte-Ambargasta (NA), Chepes–Ulapes–Los Llanos (CUL), Valle Fértil (VF), Pie de Palo (PP), Córdoba (Co), San Luis (SL).

eral distribution from which two mineralogical/microstructural domains are recognized: (i) andalusite-bearing domains (staurolite–biotite–garnet–andalusite; Fig. 2a–d) and (ii) cordierite-bearing domains (biotite–garnet–cordierite ± staurolite; Fig. 2e,f). The quartz–plagioclase–phyllosilicate-rich matrix shows a dominant

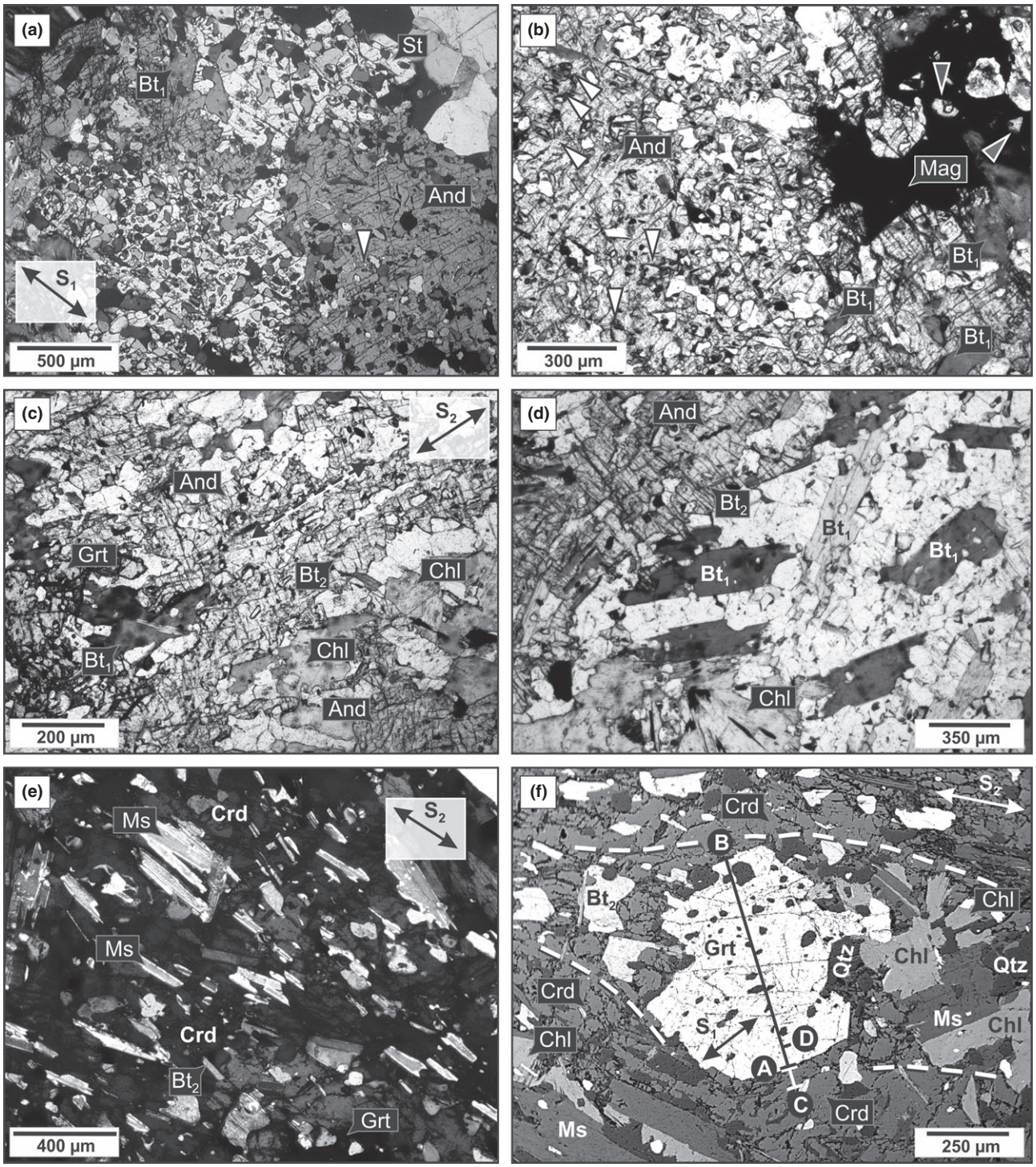

Fig. 2. Microphotographs of staurolite–biotite–garnet–cordierite–andalusite–quartz–muscovite schists from the Ancasti metamorphic complex (sample ANC-19000). (a–d) corresponds to andalusite-bearing domains. (a) Staurolite poikiloblast partially replaced by an andalusite poikiloblast. Inclusion of staurolite in andalusite is indicated by a white triangle. Both poikiloblasts showing similar patterns of aligned inclusions suggesting a relict S_1 early foliation. (b) Details of an andalusite poikiloblast and its intergrowth with magnetite. Inclusions of staurolite are observed in both andalusite and magnetite, indicated by triangles. (c) Rim zone of the andalusite poikiloblast showing inclusions of biotite (Bt_2) flakes aligned along S_2. (d) Decussate biotite (Bt_1) poikiloblasts near an andalusite poikiloblast showing aligned inclusions of Bt_2 and opaque minerals parallel to S_2. (e–f) corresponds to cordierite-bearing domains. (e) Aggregate of cordierite poikiloblasts with inclusions of muscovite and biotite (Bt_2) aligned with S_2 foliation. (f) Inclusion of garnet in cordierite poikiloblast showing preservation of pressure shadows coherent with garnet growth being pre-S_2 and cordierite post-S_2.

foliation defined by aligned flakes of muscovite and minor biotite that wraps around staurolite, garnet and biotite porphyroblasts.

Biotite and muscovite

Biotite is the most abundant mineral in this rock and occurs in two microstructural varieties: one (Bt_1; Fig. 2a–d; abbreviations after Kretz, 1983) is mainly present as millimetre-sized poikiloblasts (up to 3 mm in size) of subhedral shape, commonly containing linear trails of small rounded inclusions of quartz, ilmenite and zircon with pleochroic halos that define an internal foliation (S_1). The other variety (Bt_2; Fig. 2e,f) is scarce and occurs as small thin flakes (up to 0.5 mm) aligned in the matrix foliation (S_2). Bt_1 is pre-tectonic and Bt_2 is syn-tectonic with respect to S_2. The Bt_1 poikiloblasts are partially replaced by chlorite and muscovite.

Muscovite occurs in as aligned, subhedral, thin flakes (up to 0.6 mm in size; Fig. 2e) along the matrix foliation S_2.

Biotite and muscovite grains frequently show an internal deformation of variable intensity, with kinking and folding of phyllosilicate flakes.

Garnet

Garnet porphyroblasts (up to 1 mm in size) were recognized as subhedral grains in the matrix as well as euhedral inclusions in staurolite and as anhedral to subhedral inclusions in andalusite and cordierite poikiloblasts (Fig. 2f). The irregular shape of garnet included in the porphyroblasts suggests partial resorption of the garnet. Straight patterns of small rounded and elongated inclusions (S_1) of quartz and scarce ilmenite are commonly present in garnet.

Staurolite

Staurolite occurs as non-oriented euhedral to subhedral poikiloblasts (up to 2 cm in size; Figs 1d & 2a), with straight patterns of small rounded inclusions of quartz defining an internal foliation (S_1). Furthermore, inclusions of biotite poikiloblast (Bt_1), subhedral to euhedral garnet, ilmenite and tourmaline were recognized inside staurolite. The staurolite is partially replaced by poikiloblastic andalusite (Fig. 2a,b).

Cordierite

Cordierite occurs as anhedral irregular to ovoid poikiloblasts (up to 2 cm in size; Figs 1d & 2e,f) that are elongated subparallel to the external foliation (S_2). The poikiloblasts contain aligned inclusions of muscovite and biotite (Bt_2) continuous with the external foliation (Fig. 2e). In addition, scarce garnet and biotite (Bt_1) poikiloblasts, quartz, plagioclase, zircon with weak pleochroic halos, apatite, tourmaline and rutile were recognized as inclusions in cordierite, as well as inclusions of garnet with strain shadows composed of quartz and biotite (partially replaced by muscovite and chlorite) (Fig. 2f). Thus, cordierite growth is interpreted as late syn- to post-tectonic with respect to the development of the matrix foliation S_2. Cordierite often shows pinnite alteration in the rims.

Andalusite

Andalusite occurs as anhedral to subhedral poikiloblasts of up to 1 cm in size (Fig. 2a), with core inclusions of staurolite, biotite (Bt_1), ilmenite, quartz and magnetite (the latter with internal inclusions of staurolite); this resembles the mineral inclusion pattern in staurolite (Fig. 2a,b). Inclusions near the rim of andalusite poikiloblasts are coarser than those found in their cores and mainly consist of quartz, plagioclase and scarce Bt_2. The Bt_2 flakes display a remarkable parallelism with mica flakes defining the matrix foliation S_2 (Fig. 2c,d).

DEFORMATION–CRYSTALLIZATION RELATIONSHIPS

Figure 3 shows a schematic reconstruction of these relations (Fig. 3e) for the St–Bt–Grt–Crd–And schist. Bt_1, garnet and staurolite poikiloblasts grew synchronously and overprinted an earlier foliation S_1 linked to M_1 metamorphic event (Fig. 3a,b): the relict foliation S_1 included in these minerals, mainly represented by straight patterns of small rounded inclusions of quartz, shows a similar and constant orientation and suggests that these minerals are related to the same thermal episode (M_2 metamorphic event; previously named as M_3 by Willner, 1983b) and that this event is pre-, syn- and post-tectonic with respect to S_2. Thus, staurolite, biotite, garnet together plagioclase and quartz from the matrix constitute the peak metamorphic assemblage for M_2 event. An early muscovite likely formed part of this assemblage, but this muscovite is not preserved and would be completely recrystallized as new muscovite. The static mineral growth during M_2 is overprinted by the D_2 episode with growth of muscovite and scarce biotite (Bt_2) aligned with the S_2 foliation (Fig. 3c). Andalusite and cordierite are late syn- to post-tectonic with respect to foliation S_2 (Fig. 3d). The phyllosilicates were subsequently deformed and some crystals developed kinking and folding (not represented in Fig. 3).

MINERAL COMPOSITION

Several minerals were analysed to characterize the compositional variations critical for mineral equilibrium modelling (Tables 1 & S1). The analyses were performed with a JEOL JXA 8900M microprobe at the Universidad Complutense de Madrid (Spain), operating in WDS mode, under 15 kV accelerating potential, 20 nA beam current and a diameter of the beam of 5 μm.

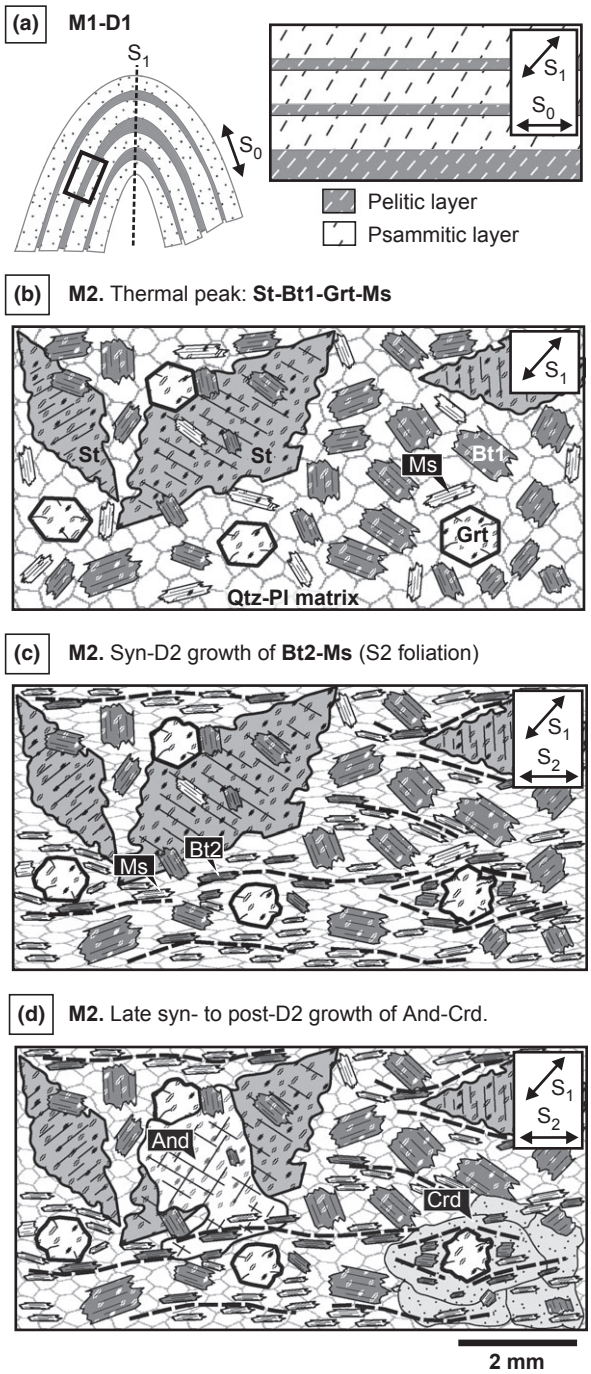

A representative profile for garnet included in cordierite is shown in Fig. 4a. This garnet exhibits two distinguishable compositional zones: a flat core zone and a zoned narrow rim. The core zone is characterized by a flat profile in Ca, Mn, Mg, Fe with XFe [XFe = Fe/(Fe + Mg) = 0.84, Prp = 0.12, Alm = 0.65, Grs = 0.06–0.07 and Sps = 0.16]. The rim displays slight compositional variations with higher spessartine (Sps = 0.20) and lower grossular (Grs = 0.05), pyrope (Prp = 0.11) and almandine (Alm = 0.67–0.63 from internal to external rim zone) (Fig. 4a). This rim is almost absent in garnet included in poikiloblastic andalusite that display flat profiles in almandine (Alm = 0.66), pyrope (Prp = 0.10–0.12) and grossular (Grs = 0.06–0.07) and only a slight increase in the spessartine content of the rim (Sps core = 0.16; Sps rim = 0.19). The flat compositional patterns shown by the core zones of garnet are interpreted here to be related to homogenization at high-T, so that the garnet composition in the internal flat segment may be a good approximation to that near-peak M_2 P–T conditions, whereas the rim may represent the results of retrograde exchange reaction, for example, with the cordierite host.

The cordierite typically shows XFe 0.29–0.32 and low Na values of up to 0.10 a.p.f.u. Slight variations in XFe were recognized near the interface between one of the garnet inclusions and its cordierite host, with cordierite values of XFe = 0.30 near the garnet and XFe = 0.28 away from it (see Fig. 4b).

Staurolite porphyroblast profiles display almost homogeneous XFe compositions of 0.78–0.81 (Fig. 4c), and ZnO contents of 0.3–0.67 wt%. Staurolite compositions measured at < 100 μm from the contact with an inclusion of biotite (see profiles of Fig. 4c,d) and from the contact with matrix biotite show high XFe values (0.80–0.83). The most ferrous compositions were found in staurolite inclusions inside andalusite, having values of XFe 0.85–0.88 and ZnO of 0.4–0.5 wt%. A staurolite included in magnetite shows XFe 0.81 and ZnO of 0.5 wt%.

The poikiloblastic biotite (Bt_1) shows XFe values that range between 0.42 and 0.49 and Ti values between 0.14 and 0.20 a.p.f.u. Measured differences in composition have been detected and related to microstructural position as follows: (i) inclusions of biotite flakes within cordierite have XFe 0.42–0.44 and Ti 0.14–0.18 a.p.f.u.; (ii) biotite in contact with cordierite has XFe 0.47 and Ti 0.19 a.p.f.u.; (iii) inclusions of

Fig. 3. Schematic microstructural reconstructions of the deformation-metamorphic mineral growth history for the metapelitic staurolite–biotite–garnet–cordierite–andalusite schist (see text). (a) M_1–D_1, evidenced by inclusions of Qtz + Op aligned. (b–d) M_2 event, from pelitic layer in (a): (b) thermal peak on a pelitic layer with static growth of St–Bt_1–Grt–Ms, (c) D_2 episode and development of S_2 foliation with syn-D_2 growth of Bt_2–Ms, (d) decompression stage, with late syn- to post-D_2 growth of andalusite and cordierite. (e) Stability ranges of major constituent minerals.

Table 1. Selected microprobe analyses of minerals from ANC-19000 sample.

Mineral	Garnet					Cordierite					Plagioclase		
Site	In Crd A–B profile (see Fig. 2f)			In andalusite		Crd–Grt contact (A–C profile, Fig. 2f)			Porphyroblast				
	External rim	Internal rim	Core	Rim	Core	External rim	Internal rim	Core	Rim	Core			
Analysis	Grt-4	Grt-8	Grt-35	Grt-301	Grt-306	Crd-18	Crd-21	Crd-29	Crd-87	Crd-93	Analysis	Pl-333	Pl-335
Wt%											Wt%		
SiO_2	37.38	36.99	37.13	37.04	37.72	48.90	49.12	48.93	47.92	48.36	SiO_2	61.00	61.10
TiO_2	< 0.08	< 0.08	< 0.08	< 0.08	< 0.08	< 0.08	< 0.08	< 0.08	< 0.08	< 0.08	TiO_2	< 0.08	< 0.08
Al_2O_3	21.46	21.39	21.39	21.09	21.36	32.53	32.95	32.11	32.60	31.82	Al_2O_3	23.96	24.70
Cr_2O_3	< 0.06	< 0.06	< 0.06	< 0.06	< 0.06	< 0.06	< 0.06	< 0.06	< 0.06	< 0.06	Cr_2O_3	< 0.06	< 0.06
FeO	28.15	29.58	29.31	29.24	29.06	6.50	6.21	6.40	6.93	6.93	FeO	< 0.08	< 0.08
MnO	8.94	7.44	7.27	7.61	6.92	0.50	0.49	0.60	0.30	0.37	MnO	< 0.08	< 0.08
MgO	2.72	2.84	3.05	2.69	3.03	8.65	9.05	8.47	8.58	8.27	MgO	< 0.04	< 0.04
CaO	1.79	2.01	2.35	2.09	2.18	< 0.04	< 0.04	< 0.04	< 0.04	0.04	CaO	6.23	6.48
Na_2O						0.46	0.47	0.39	< 0.03	0.03	Na_2O	8.37	8.24
K_2O						< 0.03	< 0.03	< 0.03	< 0.03	0.32	K_2O	0.08	0.05
Total	100.45	100.24	100.49	99.77	100.26	97.55	98.29	96.90	96.34	96.14	Total	99.65	100.57
Oxygen	24	24	24	24	24	18	18	18	18	18	Oxygen	32	32
Si	5.99	5.95	5.95	5.99	6.03	5.04	5.02	5.08	5.01	5.07	Si	10.89	10.81
Ti											Ti		
Al	4.05	4.06	4.04	4.02	4.02	3.95	3.97	3.93	4.01	3.93	Al	5.04	5.15
Cr											Cr		
Fe^{2+}	3.77	3.98	3.93	3.95	3.88	0.56	0.53	0.55	0.60	0.61	Fe^{2+}		
Mn	1.21	1.01	0.99	1.04	0.94	0.04	0.04	0.05	0.03	0.03	Mn		
Mg	0.65	0.68	0.73	0.65	0.72	1.33	1.38	1.31	1.34	1.29	Mg		
Ca	0.31	0.35	0.40	0.36	0.37					0.00	Ca	1.19	1.23
Zn											Zn		
Na						0.09	0.09	0.08		0.01	Na	2.90	2.83
K										0.04	K	0.02	0.01
Sum	15.98	16.02	16.03	16.01	15.96	11.03	11.04	11.00	10.99	10.99	Sum	20.04	20.03
XFe	0.85	0.85	0.84	0.86	0.84	0.30	0.28	0.30	0.31	0.32			
Xprp	0.11	0.11	0.12	0.11	0.12						Or	0	0
Xalm	0.63	0.66	0.65	0.66	0.66						Ab	71	70
Xgrs	0.05	0.06	0.07	0.06	0.06						An	29	30
Xsps	0.20	0.16	0.16	0.17	0.16								

Mineral	Staurolite										
Site	Andalusite domain	Bt–St contact		St in And	St in Mag	E–F profile (see Fig. 4c,d)		G–H profile (see Fig. 4c,d)			Near to cordieritic domain
		External rim	Internal rim			Core	Rim	Rim	Core	Rim	
Analysis	St-67	St-122	St-124	St-134	St-106	St-369	St-351	St-353	St-360	St-368	St-67
Wt%											
SiO_2	27.76	27.30	27.37	27.10	27.16	27.76	27.79	27.84	27.84	27.84	27.76
TiO_2	0.61	0.62	0.65	0.69	0.62	0.67	0.58	0.59	0.66	0.56	0.61
Al_2O_3	53.16	53.25	53.03	53.62	52.97	53.97	54.13	54.00	53.81	53.66	53.16
Cr_2O_3	< 0.06	0.09	< 0.06	< 0.06	< 0.06	< 0.06	< 0.06	< 0.06	< 0.06	< 0.06	< 0.06
FeO	12.55	12.92	12.54	12.18	12.38	12.87	12.66	12.94	12.58	12.65	12.55
MnO	0.38	0.52	0.42	0.56	0.44	0.46	0.44	0.40	0.37	0.47	0.38
MgO	1.87	1.52	1.78	1.06	1.60	1.95	1.89	1.96	1.81	1.98	1.87
CaO	< 0.04	< 0.04	< 0.04	< 0.04	< 0.04	< 0.04	< 0.04	< 0.04	< 0.04	< 0.04	< 0.04
ZnO	0.29	0.24	0.30	0.41	0.50	0.55	0.49	0.55	0.54	0.56	0.29
Na_2O	0.11	0.14	0.14	0.18	0.19	0.05	0.04	0.05	0.04	0.04	0.11
K_2O	< 0.03	< 0.03	< 0.03	< 0.03	< 0.03	< 0.03	< 0.03	< 0.03	< 0.03	< 0.03	< 0.03
Total	96.73	96.59	96.23	95.80	95.86	98.28	98.02	98.33	97.64	97.76	96.73
Oxygen	46	46	46	46	46	46	46	46	46	46	46
Si	7.77	7.68	7.71	7.66	7.69	7.67	7.69	7.69	7.73	7.73	7.77
Ti	0.13	0.13	0.14	0.15	0.13	0.14	0.12	0.12	0.14	0.12	0.13
Al	17.54	17.65	17.60	17.86	17.67	17.58	17.64	17.58	17.60	17.55	17.54
Cr		0.02									
Fe^{2+}	2.94	3.04	2.95	2.88	2.93	2.97	2.93	2.99	2.92	2.94	2.94
Mn	0.09	0.12	0.10	0.13	0.11	0.11	0.10	0.09	0.09	0.11	0.09
Mg	0.78	0.64	0.75	0.45	0.67	0.80	0.78	0.80	0.75	0.82	0.78
Ca											
Zn	0.06	0.05	0.06	0.09	0.10	0.11	0.10	0.11	0.11	0.11	0.06
Na	0.06	0.08	0.08	0.10	0.11	0.03	0.02	0.03	0.02	0.02	0.06
K											
Sum	29.36	29.40	29.39	29.31	29.40	29.41	29.38	29.42	29.35	29.39	29.36
XFe	0.79	0.83	0.80	0.87	0.81	0.79	0.79	0.79	0.80	0.78	0.79

Table 1. (*Continued*)

Mineral	Biotite (Bt1)							Biotite (Bt2)		Chlorite (after biotite)		Muscovite	
Site	Bt–St contact	Bt in St	Bt in Crd	Bt–Crd contact	Bt in And	Bt–Mag contact	Bt in matrix	Bt in And	Bt in Crd	Chl–Crd contact	Chl in Crd	Ms in matrix	Ms in Crd
Analysis	Bt-118	Bt-145	Bt-28	Bt-82	Bt-107	Bt-105	Bt-140	Bt-317	Bt-318	Chl-76	Chl-92	Ms-245	Ms-324
Wt%													
SiO_2	36.43	36.13	36.68	36.15	35.41	35.05	35.88	36.56	36.69	25.34	24.97	46.66	46.05
TiO_2	1.55	1.42	1.55	1.72	1.30	1.56	1.77	1.90	0.77	0.12	0.11	0.30	0.6
Al_2O_3	19.17	19.58	19.97	19.25	19.44	18.90	19.60	20.27	20.40	23.61	24.17	37.06	35.9
Cr_2O_3	< 0.06	< 0.06	0.13	< 0.06	0.08	< 0.06	0.09	0.11	0.14	0.08	< 0.06	< 0.06	< 0.06
FeO	16.46	15.99	15.33	17.06	16.30	17.00	16.97	16.42	16.03	20.51	19.62	1.03	0.94
MnO	0.11	0.11	0.20	0.08	0.09	0.12	0.18	0.11	0.17	0.21	0.13	< 0.08	< 0.08
MgO	11.32	12.15	10.86	10.82	11.32	11.39	10.72	10.17	11.78	16.76	16.36	0.47	0.59
CaO	< 0.04	0.13	< 0.04	< 0.04	< 0.04	< 0.04	< 0.04	0.06	0.04	< 0.04	< 0.04	0.03	0.02
Na_2O	< 0.03	< 0.03	0.29	< 0.03	< 0.03	< 0.03	< 0.03	0.28	0.35	< 0.03	< 0.03	1.39	1.33
K_2O	8.57	8.25	8.66	9.03	8.74	8.89	8.60	8.81	9.07	< 0.03	0.12	9.22	9.54
F	0.16	0.17	0.19	0.17	0.22	0.13	0.19	0.18	0.20	< 0.09	< 0.09	< 0.09	< 0.09
Cl	< 0.02	< 0.02	< 0.02	< 0.02	< 0.02	< 0.02	< 0.02	< 0.02	0.02	< 0.02	< 0.02	< 0.02	< 0.02
Total	93.77	93.93	93.75	94.28	92.80	93.04	93.92	94.79	95.57	86.63	85.48	96.16	94.97
Oxygen	21	21	21	21	21	21	21	21	21	28	28	21	21
Si	5.48	5.41	5.50	5.46	5.00	5.37	5.41	5.46	5.44	5.25	5.23	6.09	6.12
Al^{IV}	2.52	2.59	2.50	2.54	3.00	2.63	2.59	2.54	2.56	2.23	2.04	1.91	1.88
Al^{VI}	0.88	0.86	1.03	0.88	0.24	0.79	0.90	1.03	1.01	3.54	3.92	3.79	3.73
Ti	0.18	0.16	0.17	0.19	0.14	0.18	0.20	0.21	0.09	0.02	0.02	0.03	0.06
Cr	0.00	0.01	0.01	0.00	0.01	0.00	0.01	0.01	0.02	0.01			
Fe^{2+}	2.07	2.00	1.92	2.15	1.93	2.18	2.14	2.05	1.99	3.56	3.43	0.11	0.11
Mn	0.01	0.01	0.02	0.01	0.01	0.02	0.02	0.01	0.02	0.04	0.02		
Mg	2.54	2.71	2.43	2.44	2.38	2.60	2.41	2.26	2.61	5.18	5.11	0.09	0.12
Ca		0.02						0.01	0.01			0.00	0.00
Na			0.08					0.08	0.10			0.35	0.34
K	1.65	1.58	1.66	1.74	1.58	1.74	1.66	1.68	1.72		0.03	1.54	1.62
F	0.07	0.08	0.09	0.08	0.10	0.06	0.09	0.09	0.09				
Cl									0.01				
Sum	15.40	15.43	15.43	15.50	14.38	15.58	15.43	15.34	15.56	19.84	19.80	13.92	13.98
XFe	0.45	0.42	0.44	0.47	0.45	0.46	0.47	0.48	0.43	0.41	0.40	0.55	0.47
XNa = Na/(Na + Ca + K)												0.17	0.17

Mineral	Ilmenite			
Site	In Crd	In Crd	Matrix	In St
Analysis	Ilm-99	Ilm-50	Ilm-236	Ilm-65
Wt%				
SiO_2	< 0.06	< 0.06	< 0.06	0.08
TiO_2	55.05	58.39	53.82	59.62
Al_2O_3	< 0.05	0.11	< 0.05	0.09
Cr_2O_3	< 0.06	< 0.06	< 0.06	< 0.06
FeO	41.33	35.15	41.22	32.32
MnO	3.37	2.85	2.80	0.67
MgO	0.08	0.08	0.08	0.19
BaO	0.33	0.38		0.37
Total	100.16	96.97	97.92	93.34
Oxygen	6	6	6	6
Si				0.00
Ti	2.06	2.19	2.06	2.28
Al		0.01		0.01
Cr				
Fe^{2+}	1.72	1.47	1.75	1.37
Mn	0.14	0.12	0.12	0.03
Mg	0.01	0.01	0.01	0.01
Ba	0.01	0.01		0.01

<: less than the stated detection limit (at 2σ). An element was considered present if its concentration exceeded twice the calculated detection limit.
Xprp = Mg/(Mg + Ca + Mn + Fe); Xalm = Fe/(Mg + Ca + Mn + Fe); Xgrs = Ca/(Mg + Ca + Mn + Fe); Xsps = Mn/(Mg + Ca + Mn + Fe).

biotite flakes within andalusite have XFe 0.45 and Ti 0.14 a.p.f.u.; (iv) a biotite in contact with magnetite has XFe 0.46 and Ti 0.18 a.p.f.u.; (v) a biotite poikiloblast from the matrix has inside values of XFe of 0.46–0.49 and of Ti 0.18–0.20 a.p.f.u. but XFe 0.45–0.46 with the same values for Ti near its contact with a staurolite porphyroblast; and (vi) an inclusion of biotite poikiloblast within staurolite has XFe 0.42–0.44 and Ti 0.16–0.19 a.p.f.u. The Bt_2 included in andalusite poikiloblasts has a composition of XFe 0.48–0.50 and Ti

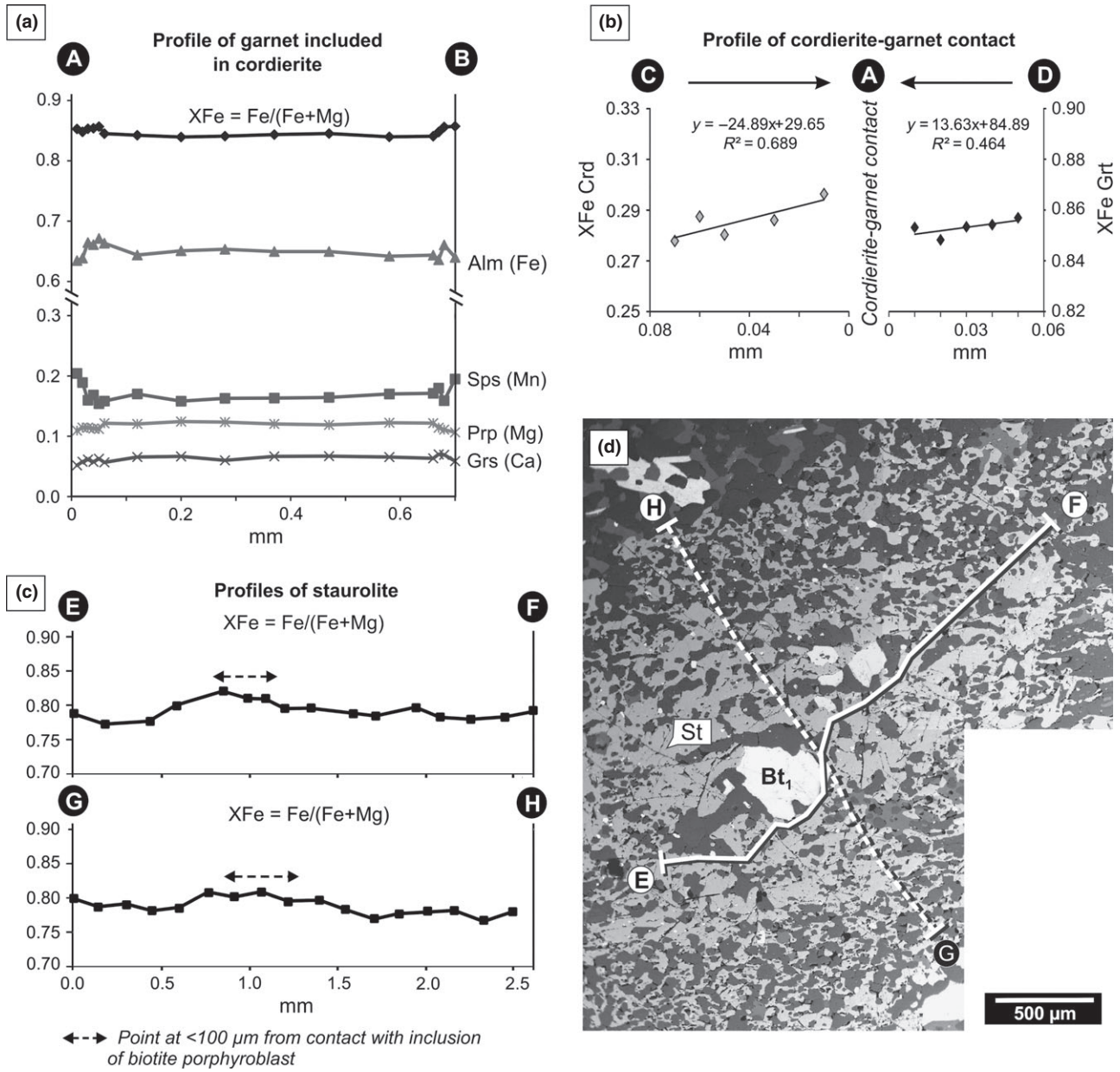

Fig. 4. (a) Compositional profile in subhedral garnet included in cordierite (see Fig. 2f for location of profiles). (b) XFe profiles for rim zone in cordierite–garnet contact. (c) XFe profiles in staurolite poikiloblasts. (d) Backscatter image shows staurolite profile locations.

contents of 0.15–0.21 a.p.f.u., and Bt_2 included in cordierite has XFe values range of 0.43–0.45 and Ti values of 0.09–0.16 a.p.f.u.

Muscovite has XFe 0.47–0.55 and XNa 0.15–0.19. Chlorite has a XFe 0.40–0.41. Plagioclase shows a composition of $An_{27–32}$. The analysed ilmenite (see Table 1) shows a Mn compositional range from 0.03 to 0.14 a.p.f.u.

MINERAL EQUILIBRIUM MODELLING

Mineral equilibrium calculations where performed in the MnNCKFMASH ($MnO–Na_2O–CaO–K_2O–FeO–MgO–Al_2O_3–SiO_2–H_2O$) system using THERMOCALC v3.33 software (Powell & Holland, 1988) and the updated version of the ds55 thermodynamic data set (November, 2003; Holland & Powell, 1998). The minerals and activity-composition models used were garnet (White *et al.*, 2005), biotite (Mahar *et al.*, 1997; Powell & Holland, 1999), staurolite and cordierite (Mahar *et al.*, 1997; Holland & Powell, 1998), muscovite (Coggon & Holland, 2002), chlorite (Holland *et al.*, 1998), plagioclase and K-feldspar (Holland & Powell, 2003). The effects of Fe^{3+} and Ti contents were not considered, mainly because a reliable Mn + Fe^{3+} model is still lacking for the majority of

the phases modelled, and because Mn was considered to have a more critical influence on mineral equilibria (e.g. for garnet) than Fe^{3+} at the pertinent metamorphic grades.

The results of mineral equilibria calculations are shown as *P–T* and *P–X* pseudosections (Figs 5, 6 & 7). The bulk composition used was obtained from a representative sample of staurolite–biotite–garnet–cordierite–andalusite–quartz–muscovite schist (ANC-19000; Table 2) by conventional XRF spectrometry (Rigaku FX2000 spectrometer, Instituto de Geología y Minería of the Universidad Nacional de Jujuy), treating all the iron as Fe^{2+} (FeOt). However, the occurrence of magnetite and ilmenite implies the presence of Fe^{3+} and hence an overestimation of the amount of available Fe^{2+}. In the MnNCKFMASH system, this would result in enlargement of the staurolite stability field at low pressure in FeO richer compositions. To reduce this effect, a molar amount of FeO equivalent to the present TiO_2 was subtracted, assuming an ideal stoichiometric distribution of Ti and Fe^{2+} (TiO_2 = FeO) in ilmenite and that all TiO_2 is assigned to this mineral (Table 2). On the other hand, the inclusion of Mn + Fe^{3+} in garnet is still waiting for development of a reliable solid solution model for low pressure and intermediate temperature such as shown in White *et al.* (2005).

P–T pseudosection calculations

A *P–T* pseudosection was constructed to estimate the *P–T* metamorphic peak condition of the main metamorphic event (M_2) in the Ancasti banded schist sample (Fig. 5). Since the calculation was made for subsolidus conditions, H_2O contents were set to saturate the *P–T* field of interest, which is considered appropriate for modelling prograde evolution in metapelitic systems before melt conditions are reached (Table 2). Biotite, quartz and plagioclase occur in all fields throughout the *P–T* range of interest and muscovite is present everywhere except in a small field where muscovite-breakdown occurs at the highest temperature and lowest pressure (Fig. 5a). Garnet shows a more restricted stability field which expands over the highest *P–T* range considered in this study (Fig. 5a). Staurolite is predicted to be stable near the highest *P–T* corner, whereas andalusite is restricted to a small stability *P–T* range (~555–600 °C and 3.5–4.1 kbar; Fig. 5a). Cordierite appears in the lower pressure to higher temperature corner (Fig. 5a). Garnet isopleths predict a decrease in spessartine along and an increase in grossular and almandine towards higher pressure (Fig. 5a). XFe = Fe/(Fe + Mg) in staurolite, biotite and cordierite vary as shown in Fig. 5b,c; in general, they decrease in XFe with increasing pressure. Measured garnet core composition isopleths (Grs = 0.06–0.07, Sps = 0.16 and Alm = 0.65), which are inferred to represent the near-peak M_2, *P–T* conditions, intersect inside the wedge-shaped 4-variant field staurolite–biotite–garnet–plagioclase–muscovite–quartz with a mean value of ~590 °C and 5.2 kbar (see white boxes in Fig. 5b,c).

Interestingly, such as pointed out in the introduction, there is not a single assemblage that embraces staurolite, biotite, garnet, cordierite, andalusite, plagioclase, muscovite and quartz all together in the *P–T* pseudosection (Fig. 5a). The staurolite-bearing stability fields lack andalusite and cordierite, whereas the lower pressure assemblages with andalusite and cordierite lack staurolite. So andalusite and cordierite must have grown subsequently in decompressional metamorphic conditions, during which the staurolite porphyroblasts now present in the sample would have remained metastable. The biotite–garnet–cordierite–andalusite–plagioclase–muscovite–quartz field occurs at lower pressure in the model pseudosection, but this occurrence still cannot account for the detailed microstructural relationships observed in the real rock sample, for example, andalusite domains without cordierite and cordierite domains without andalusite.

To sum up, pseudosection modelling using the XRF bulk rock composition could not account for the observed metamorphic evolution. Therefore, by confronting the observed microstructures and the *P–T* modelling, the existence of local equilibrium can be strongly suggested.

Pseudosection calculations for post-peak conditions: decompression P–T path

Some previous studies have shown how factors such as grain size distribution (e.g. Stüwe, 1997) and progressive chemical isolation of porphyroblast cores (e.g. Marmo *et al.*, 2002; Evans, 2004) can influence the mineralogical development during metamorphic evolution through modification of the local EBC. Thus, XRF bulk compositions are not valid for constructing model pseudosections for all stages of evolution, particularly for post-peak conditions. In this article, the evolution of sample ANC-19000 characterized by heterogeneous modal distribution of staurolite is explored, analysing the contribution of staurolite to the local bulk composition. As a first hypothesis, we assumed that during post-peak conditions only the outer shell encompassing the periphery of large staurolite porphyroblasts interacted chemically with the matrix, while the cores became chemically isolated. However, this possibility has been discarded since the XFe profiles in staurolite show, in fact, homogeneous composition (see Fig. 4c) suggesting high diffusion rates across staurolite during nearly isothermal retrogression.

Since the presence of andalusite and cordierite suggests a post-peak decompression stage (see Fig. 5a), the effect of the staurolite modal distribution on mineral development during nearly isothermal decompression was modelled to a first approximation by constructing a $P–X_{EBC}$ pseudosection diagram (Fig. 6)

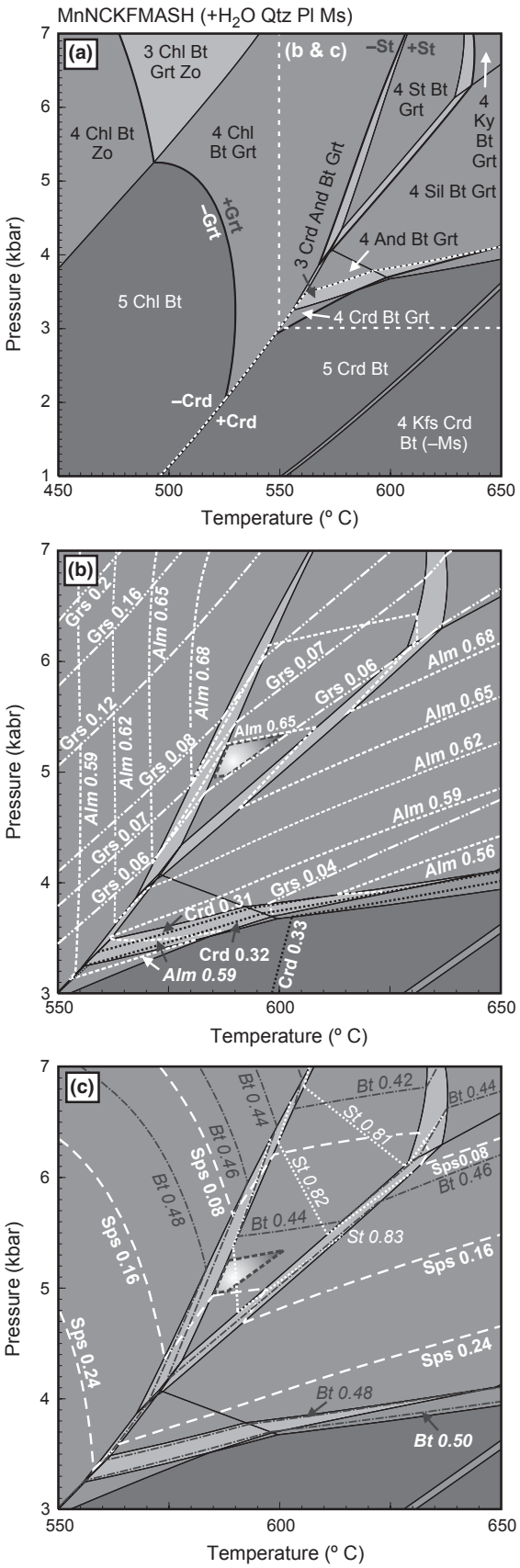

calculated at the peak temperature of 590 °C. The 4.4 mol% of staurolite at peak conditions of 590° and 5.2 kbar calculated by THERMOCALC and expressed as mole per cent, is considered to approximate volume per cent of staurolite (see Stüwe & Powell, 1995), is represented by point A (X_{EBC} = 0.2). X_{EBC} values of 0 and 1 represent extreme degrees of chemical participation of staurolite porphyroblasts in the equilibrating volume after peak conditions. Thus, a local bulk composition defined by the staurolite-free matrix (0 mol% St) is represented by X_{EBC} = 0 (point 'B' in Fig. 6), whereas X_{EBC} = 1 (Fig. 6) represents a staurolite-rich domain with 22 mol% of staurolite, where it constitutes ~1/5 of the matrix volume. This last value represents an arbitrary mode for a staurolite-rich domain chosen so that we can depict the assemblages developed under nearly isothermal decompression in domains progressively richer in staurolite. All bulk compositions – X_{EBC} = 0 (point B), X_{EBC} = 0.6 (point C) and X_{EBC} = 1 – were calculated using the rbi script of THERMOCALC from the modes obtained at 590 °C and 5.2 kbar (point A). Values for these bulk compositions are given in Table 2.

Greater modal amounts of staurolite participating in the EBC lead to higher XFe values in cordierite and biotite and to an enlargement of the andalusite stability field towards lower pressure, with concomitant reduced stability of cordierite. Thus, at, for example, 3.7 kbar, it is possible to develop two alternative local assemblages (white points in Fig. 6), either biotite–garnet–cordierite–plagioclase–muscovite–quartz for X_{EBC} = 0 or biotite–garnet–andalusite–plagioclase–muscovite–quartz for X_{EBC} = 1 (Fig. 6), which are controlled by domains with different amounts of staurolite, even in the same sample. Furthermore, XFe values of measured Bt_2 composition (0.48–0.50) from andalusite-bearing domains are predicted near X_{EBC} = 0.6, whereas ferrous values of biotite (0.43–0.47) from cordierite-bearing domain are founded near X_{EBC} = 0 (see Fig. 6).

Figure 7a displays a *P–T* pseudosection showing stable mineral assemblages in post-peak *P–T* conditions for a bulk composition without contribution of staurolite (point B, X_{EBC} = 0 from Fig. 6), whereas Fig. 7b would be valid for a bulk composition with a significant amount of staurolite of 13 mol% of staurolite (point C, X_{EBC} = 0.6, from Fig. 6). The *P–T*

Fig. 5. (a) MnNCKFMASH *P–T* pseudosection calculated for the XRF bulk composition of the representative sample of Ancasti metapelitic staurolite–biotite–garnet–cordierite–andalusite schist (ANC-19000), corrected for the presence of ilmenite (bulk composition in Table 2). Deeper shades represent higher variance assemblages. Here and elsewhere, variance is given by figures in front of each assemblage. (b–c) Enlarged inset framed by dots of the highest *P–T* part in (a) with compositional isopleths of garnet (almandine, grossular, spessartine), staurolite (XFe), biotite (XFe) and cordierite (XFe). Metamorphic peak conditions are those of the small box at ~590 °C and 5.2 kbar in (b) and (c).

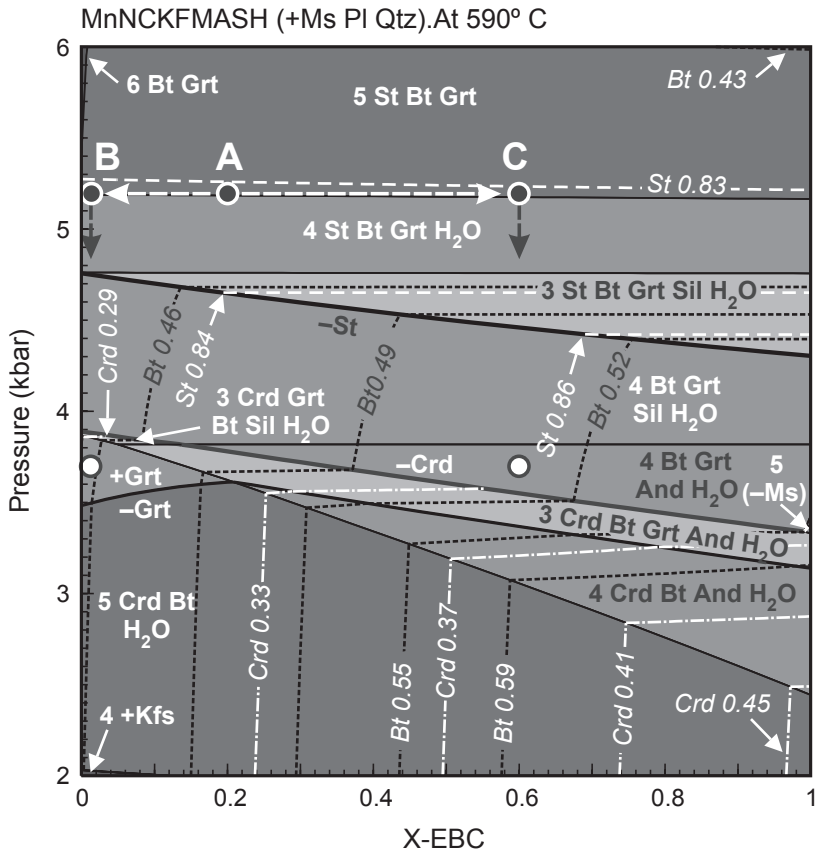

Fig. 6. MnNCKFMASH P–X_{EBC} pseudosection at 590 °C. The two compositions (X = 0 and X = 1) were calculated starting from modal values calculated by THERMOCALC for the bulk composition at peak conditions (4.4 mol% St; point 'A'). For this pseudosection, the only variable was the modal proportion of staurolite. See text for details of calculation. X_{EBC} = 0 represents an effective bulk composition (EBC) defined by a staurolite-free matrix (0 mol%; point 'B'). X_{EBC} = 1 is an EBC where staurolite markedly contributes together with matrix (22 mol% St; point 'C'). Compositional isopleths of staurolite (XFe), biotite (XFe) and cordierite (XFe) are plotted. Bulk compositions are detailed in Table 2.

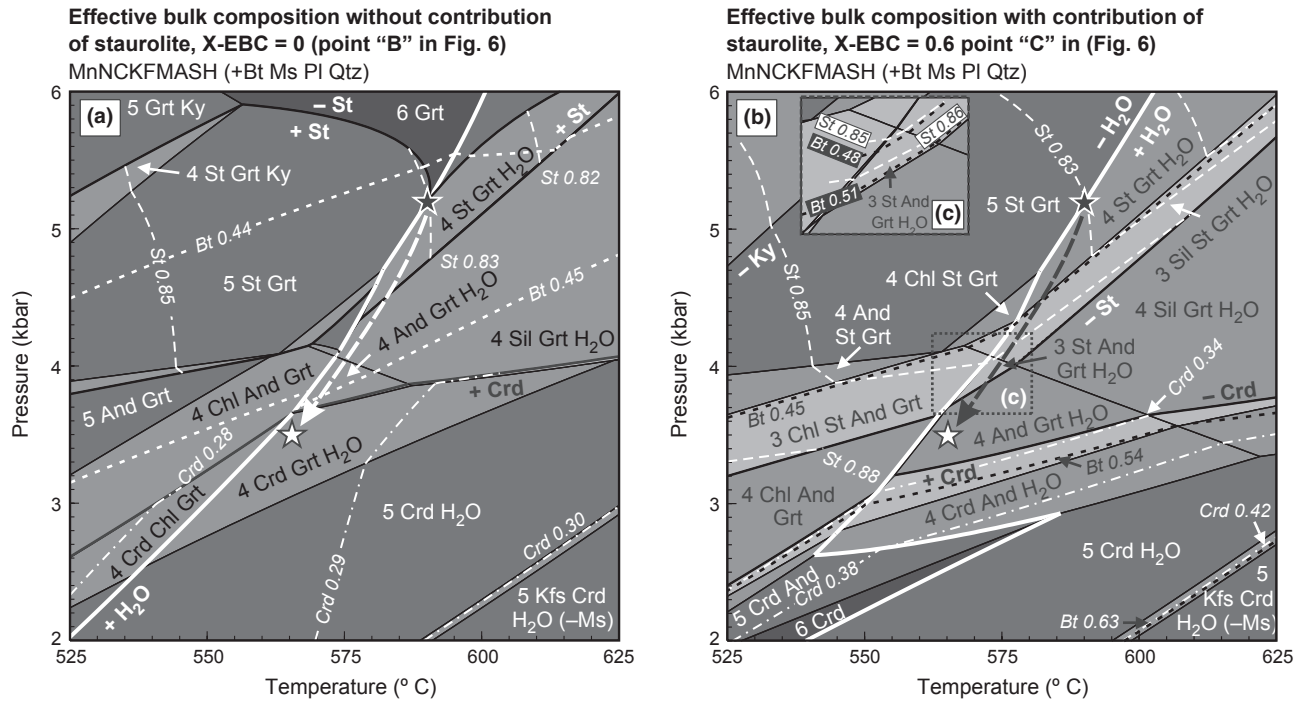

Fig. 7. MnNCKFMASH P–T pseudosections for X_{EBC} = 0 (a) and X_{EBC} = 0.6 (b) bulk compositions described in Fig. 6 (see text and Table 2). Peak and approximate post-peak P–T conditions along decompression path are indicated with white and black stars, respectively. Compositional isopleths of staurolite (XFe), biotite (XFe) and cordierite (XFe) are plotted. St–Bt–Grt–Ms–Pl–Qtz–H_2O field in P–T pseudosection for X_{EBC} = 0 (a) has a mode of staurolite of < 0.1 mol%. (c) Details of central P–T window in (b) (dotted line rectangle).

Table 2. Bulk compositions used in calculation of *P–T* and *P–X* pseudosections.

	H_2O	SiO_2	Al_2O_3	CaO	MgO	FeO	K_2O	Na_2O	MnO	TiO_2	P_2O_5	LOI	Total
Representative schist sample ANC-19000													
XRF wt%	–	59.96	18.20	0.86	4.02	7.43	4.56	1.19	0.10	0.95	0.18	1.53	98.98
Mol%[a]	–	67.63	12.10	1.04	6.76	7.00	3.28	1.30	0.10	0.80	–	–	100.0
Bulk composition used in pseudosections[a]													
In Fig. 5, Bulk corrected for ilmenite (mol%)	13.12	59.72	10.68	0.91	5.97	5.47	2.89	1.15	0.09	–	–	–	100.0
In Figs 6 and 7, $X = 0$ in $P–X_{EBC}$ pseudosection[b]	7.17	65.26	9.99	1.02	6.54	5.41	3.24	1.29	0.09	–	–	–	100.0
In Fig. 6, $X = 1$ in $P–X_{EBC}$ pseudosection[b]	7.51	58.93	15.94	0.82	5.84	7.23	2.6	1.03	0.11	–	–	–	100.0
In Fig. 7, $X = 0.6$ in $P–X_{EBC}$ pseudosection[b]	7.39	61.13	13.87	0.89	6.08	6.59	2.82	1.12	0.1	–	–	–	100.0

All the iron as FeO.

[a]Normalized oxide mole proportions at 100%.

[b]Bulk compositions for post-peak modelling were constructed using minimal H_2O contents. The derived *P–X* and *P–T* pseudosections (Figs 6 & 7) show that all post-peak evolution could have been still under water-saturated conditions because the near isothermal decompressional *P–T* path does not intersect the $-H_2O$ limit and does not enter the water-free field.

pseudosection for $X_{EBC} = 0$ (Fig. 7a) predicts a stability field with mineral assemblage characteristic of the cordierite microdomain (biotite–garnet–cordierite–plagioclase–muscovite–quartz) at ~3.5 kbar, whereas for this pressure, the *P–T* pseudosection for $X_{EBC} = 0.6$ (Fig. 7b) predicts a stability field including andalusite without cordierite (biotite–garnet–andalusite–plagioclase–muscovite–quartz). The staurolite–biotite–garnet–andalusite–plagioclase–muscovite–quartz field is predicted in the *P–T* pseudosection for $X_{EBC} = 0.6$ (Fig. 7a) where XFe isopleths for staurolite (0.85–0.86) and biotite (0.48–0.51) inside this field show values that are very similar to those measured in the real staurolite and biotite inclusions in andalusite (see Tables 1 & S1). This field would represent a real point crossed during decompression path from peak *P–T* condition (white star; Fig. 7a,b) to towards a final stability into the staurolite-absent field (biotite–garnet–andalusite–plagioclase–muscovite–quartz), located at ~565 °C and 3.5 kbar. In the *P–T* pseudosection for $X_{EBC} = 0.0$ (Fig. 7a), representative of bulk composition without contribution of staurolite, this decompression *P–T* path crosses an andalusite-absent biotite–garnet–cordierite–plagioclase–muscovite–quartz field at ~565 °C and 3.5 kbar and shows more Mg-rich chemical compositions in biotite and cordierite. All mineralogical and chemical characteristics approximate very well to those of real cordierite-rich domains in the Ancasti schist sample studied.

DISCUSSION AND FINAL COMMENTS

Widespread chemical equilibrium throughout a rock can be considered to occur only at near-peak *P–T* metamorphic conditions, so that pseudosection diagrams constructed using the appropriate XRF bulk composition would be valid only for a near-peak *P–T* window. Significant discrepancies between this model and reality, both in the identity of the equilibrium assemblage and in the composition and mode of minerals, can arise if this XRF pseudosection is used to interpret features generated far from peak *P–T* conditions. This occurs because new equilibrium volumes can develop influenced by peak microstructural relationships and mineral distribution (see Stüwe, 1997). Net transfer of matter becomes limited and diffusion rates are lower during decompression and/or cooling paths, mainly due to a decrease in temperature, and especially if interstitial fluids are not available. The fact that cooling is not important during decompression could have favoured maintaining high diffusion and exchange reaction rates in the Ancasti schists. Heterogeneous distributions of large staurolite porphyroblasts would have contributed to local modification of EBC, so that the XRF bulk composition used for modelling the peak (Fig. 5) cannot appropriately represent evolution during the post-peak stage.

The staurolite–biotite–garnet–cordierite–andalusite–quartz–muscovite schist analysed in this work shows two domains with different mineralogy: andalusite-bearing (St–Bt–Grt–And–Pl–Ms–Qtz–Ilm–Mag) and cordierite-bearing (Bt–Grt–Crd–Pl–Ms–Qtz–Ilm ± St). Microstructural observations and a *P–T* pseudosection using XRF bulk suggest that a staurolite–biotite (Bt_1)–garnet–plagioclase–muscovite–quartz association represents the peak metamorphic assemblage (Fig. 5). However, andalusite and cordierite as part of the above assemblage are not compatible within this pseudosection and represent later equilibration in two different EBCs domains according to the presence or absence of staurolite, in agreement with observed mineral distribution (see Fig. 3). In this sense, staurolite porphyroblasts would have acted as a partially metastable mineral under decompression/retrogression. Modifications to the EBC in relation to mode of staurolite at peak *P–T* conditions and spatial distribution explain the development of the domains leading to the different mineral associations for the same *P–T* conditions (Figs 6 & 7) in different areas of the same sample on a thin-section scale. Figure 8a shows four points on the decompression *P–T* path (see figure caption) drawn on the *P–T* pseudosection calculated to estimate the *P–T* metamorphic peak condition from M_2 event (see Fig. 5), where (i) is the peak at 590 °C and 5.2 kbar, (ii) represents a possible intermediate state in the *P–T* path with the rock affected by the D_2-episode, (iii) is the stability field with andalusite and staurolite in the mineral assemblage observed in petrographic analysis and compatible with measured chemical compositions in staurolite (XFe 0.85–0.88)

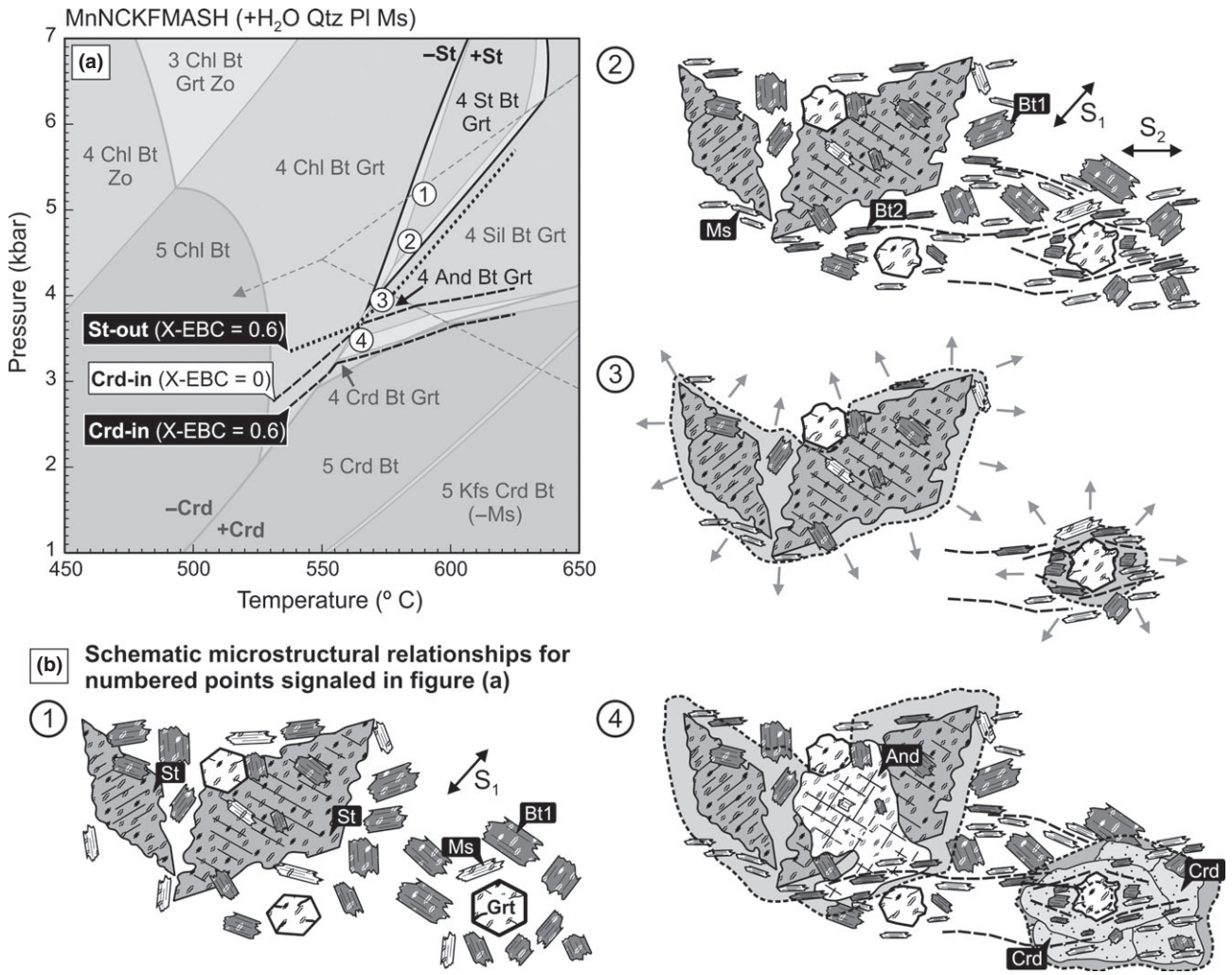

Fig. 8. (a) *P–T* pseudosection calculated for the XRF bulk composition (Fig. 5) showing segments of Crd-in and St-out stability curves from *P–T* pseudosections for $X_{EBC} = 0$ (Fig. 7a) and Crd-in from pseudosections for $X_{EBC} = 0.6$ (Fig. 7b). (b) Schematic *P–T* evolution of the microstructural relations along with evolution of the equilibration volumes during decompression *P–T* path (see text). Fourth stages are represented from peak *P–T* condition to approximate decompressional *P–T* stages indicated in Fig. 8 (a): (1) mineral assemblage and microstructure relation in equilibrium at M_2 peak *P–T* conditions (590 °C and 5.2 kbar), 4.4 mol% of St. (2) D_2 episode with development of aligned muscovite and biotite. (3) Late syn-D_2 pre-growth of cordierite and andalusite poikiloblasts. Two equilibrium volumes (grey area) are developed in different microstructural domains mainly influenced by the presence or absence of staurolite. (4) Late syn- to post-D_2 stage, in which staurolite poikiloblasts are replaced by andalusite in microdomains where the effective bulk composition (EBC) has a significant contribution of staurolite. On the other hand, cordierite grows in microdomains characterized by a reduced staurolite contribution to the EBC.

and biotite (Bt_2, XFe 0.48–0.50) included in andalusite (see Fig. 7b), and (iv) is the approximate decompressional *P–T* stage at 565 °C and 3.5 kbar (see Fig. 7). A schematic microstructural evolution along these four stages is represented in Fig. 8b, together with the influence of mineral distribution on the succession of equilibrium volumes (grey area in Fig. 8b). Andalusite-bearing and cordierite-bearing domains for the same *P–T* conditions are both possible in the same sample due to the EBC being constrained locally only by near-peak staurolite mode variations. In fact, this satisfactorily explains observed differences in mineral assemblage, modes and chemical composition of minerals.

Thus, in general, there is pretty good agreement between the compositions of analysed phases and compositions predicted from modelling and plotted as selected isopleths in the *P–T* pseudosections. Nevertheless, the staurolite composition predicted in the *P–T* pseudosection for peak conditions (XFe 0.83; Fig. 5) is more ferrous than the analyses of real staurolite (XFe 0.78–0.81). Moreover, the chemical composition of real staurolite inclusions in andalusite are predicted in the staurolite–andalusite-bearing assemblage field in *P–T* pseudosection for $X_{EBC} = 0.6$ (Fig. 7b). Analysed values of XFe in staurolite (0.79–0.80) were reproduced from the staurolite–muscovite–biotite–quartz–plagioclase assemblage at 3.5 kbars and 565 °C

modelling with THERMOCALC in P–T projection mode. These conditions are those of a decompressional stage. On the other hand, these compositions are not reproduced in P–T projections for the andalusite- and cordierite–andalusite-bearing assemblages showing staurolite with XFe values of 0.84 and 0.85, respectively. This suggests either that other factors such as the presence of Fe-bearing opaque minerals with XFe values higher than those of staurolite may have been involved in retrogression partitioning of Fe detriment of staurolite, and/or that components like Ti, Zn, Fe^{3+} have been omitted in the a–x models.

This work shows that the presence of the mineral association of staurolite, biotite, garnet, cordierite, andalusite, plagioclase, muscovite and quartz in our sample could be explained by a decompression/retrograde P–T path on the basis of development of limited equilibrium volumes consistent with our detailed microstructural observations. This could be part of a single low-P metamorphic event as an alternative interpretation to previous studies on the Ancasti metamorphic complex, where Willner (1983b) and Baldo *et al*. (2008) suggested polymetamorphism as the cause of development of this mineral assemblage. Vernon *et al*. (2008) assumed polymetamorphism if a peak assemblage for a metamorphic event is overprinted by at least a single subsequent metamorphic event at different P–T conditions. However, polymetamorphism is difficult to detect from petrological analysis alone, without support of geochronological techniques (e.g. Zeh *et al*., 2004; Berman *et al*., 2007). Therefore, a more detailed analysis, establishing thermochronological constraints along the decompression path, would be useful in confirming our interpretation and inferring the regional implications.

ACKNOWLEDGEMENTS

Financial support for this work was provided by Argentine Grants PICT-1200 BID 2437/OR-AR of FONCyT, PIP-1940 of CONICET and Spanish MEC Grants CGL2009-07984 and CGL2010-21298. Dr. R. Pankhurst is specially thanked for his suggestions. G. N. Stoessel is thanked for his contribution in field trips. We acknowledge comments by Drs Stüwe and Pitra for their constructive comments that enabled us to improve the manuscript.

REFERENCES

Ali, A., 2010. The tectono-metamorphic evolution of the Balcooma Metamorphic Group, north-eastern Australia: a multidisciplinary approach. *Journal of Metamorphic Geology*, **28,** 397–422.

Baldo, E.G., Stoessel, N., Murra, J.A. & Dahlquist, J.A., 2008. Estructuras sedimentarias en los esquistos de la Formación Ancasti: reinterpretación de la evolución tectonotérmica. *Actas del XVII Congreso Geológico Argentino*, Jujuy, **4,** 1481–1482.

Berman, R.G., Ryan, J.J., Gordey, S.P. & Villeneuve, M., 2007. Permian to Cretaceous polymetamorphic evolution of the Stewart River region, Yukon-Tanana terrane, Yukon, Canada: P-I evolution linked with in situ SHRIMP monazite geochronology. *Journal of Metamorphic Geology*, **25,** 803–827.

Coggon, R. & Holland, T.J.B., 2002. Mixing properties of phengitic micas and revised garnet-phengite thermobarometers. *Journal of Metamorphic Geology*, **20,** 683–696.

Connolly, J.A.D., 1990. Multivariable phase-diagrams – an algorithm based on generalized thermodynamics. *American Journal of Science*, **290,** 666–718.

Dahlquist, J.A., Rapela, C.W., Pankhurst, R.J. *et al*., 2012. Age and magmatic evolution of the famatinian granitic rocks of sierra de Ancasti, Sierras Pampeanas, NW Argentina. *Journal of South American Earth Sciences*, **34,** 10–25.

Evans, T.P., 2004. A method for calculating effective bulk composition modification due to crystal fractionation in garnet-bearing schist: implications for isopleth thermobarometry. *Journal of metamorphic Geology*, **22,** 547–557.

García-Casco, A. & Torres-Roldán, R.L., 1999. Natural metastable reactions involving garnet, staurolite and cordierite: implications for petrogenetic grids and the extensional collapse of the Betic-Rif Belt. *Contributions to Mineralogy and Petrology*, **136,** 131–153.

Holland, T.J.B. & Powell, R., 1998. An internally consistent thermodynamic dataset for phases of petrological interest. *Journal of Metamorphic Geology*, **16,** 309–343.

Holland, T.J.B. & Powell, R., 2003. Activity-composition relations for phases in petrological calculations: an asymmetric multicomponent formulation. *Contributions to Mineralogy and Petrology*, **145,** 492–501.

Holland, T.J.B., Baker, J.M. & Powell, R., 1998. Mixing properties and activity – composition relationships of chlorites in the system MgO-FeO-Al_2O_3-SiO_2-H_2O. *European Journal of Mineralogy*, **10,** 395–406.

Jeřábek, P., Janák, M., Faryad, W., Finger, F. & Konečný, P., 2008. Polymetamorphic evolution of pelitic schists and evidence for Permian low-pressure metamorphism in the Vepor Unit, West Carpathians. *Journal of metamorphic Geology*, **26,** 465–485.

Knüver, M., 1983. Dataciones radimétricas de rocas plútonicas y metamórficas. In: *La geología de la Sierra de Ancasti* (eds Aceñolaza, F.G., Miller, H. & Toselli, A.), *Munster, Munstersche Forschungen zur Geologie und Paleontologie*, **59,** 201–218.

Knüver, M. & Miller, H., 1981. Ages of metamorphic and deformational events in Sierra de Ancasti (Pampean Ranges, Argentina). *Geologische Rundschan*, **70,** 1020–1029.

Kretz, R., 1983. Symbols for rock forming minerals. *American Mineralogist*, **68,** 277–279.

Lottner, U., 1983. Las pegmatitas de la Sierra de Ancasti. In: *La geología de la Sierra de Ancasti* (eds Aceñolaza, F.G., Miller, H. & Toselli, A.), *Munster, Munstersche Forschungen zur Geologie und Paleontologie*, **59,** 137–151.

Mahar, E.M., Baker, J.M., Powell, R., Holland, T.J.B. & Howell, N., 1997. The effect of Mn on mineral stability in metapelites. *Journal of Metamorphic Geology*, **15,** 223–238.

Marmo, B.A., Clarke, G.L. & Powell, R., 2002. Fractionation of bulk composition due to porphyroblast growth: effects on eclogite facies mineral equilibria, Pam Peninsula, New Caledonia. *Journal of Metamorphic Geology*, **20,** 151–165.

Miró, R., Gaido, F., Candiani, J. & Aimar, C., 2004. Hoja geológica Recreo, 2966-IV, 1:250.000. *Instituto de Geología y Recursos Minerales, SEGEMAR*, 84 pp.

Murra, J.A., Baldo, E.G., Galindo, C. *et al*., 2011. Sr, C and O isotope composition of marbles from the Sierra de Ancasti, Eastern Sierras Pampeanas, Argentina: age and constraints for the Neoproterozoic–Lower Paleozoic evolution of the proto-Gondwana margin. *Geologica Acta*, **9,** 79–92.

Pankhurst, R.J. & Rapela, C.W., 1998. The proto-andean margin of Gondwana: an introduction. In: *The Proto-Andean Margin of Gondwana* (eds Pankhurst, R.J. & Rapela, C.W.) *Geological Society of London*, Special Publication, **142,** 1–9.

Pattison, D.R.M., Spear, F.S. & Cheney, J.T., 1999. Polymetamorphic origin of muscovite + cordierite + staurolite + biotite assemblages; implications for the metapelitic petrogenetic grid and for P-T paths. *Journal of Metamorphic Geology*, **17,** 685–703.

Powell, R. & Holland, T.J.B., 1988. An internally consistent thermodynamic dataset with uncertainties and correlations. 3. Application, methods, worked examples and a computer program. *Journal of Metamorphic Geology*, **6,** 173–204.

Powell, R. & Holland, T.J.B., 1999. Relating formulations of the thermodynamics of mineral solid solutions: activity modeling of pyroxenes, amphiboles, and micas. *American Mineralogist*, **84,** 1–14.

Powell, R. & Holland, T.J.B., 2008. On thermobarometry. *Journal of Metamorphic Geology*, **26,** 155–179.

Powell, R., Holland, T. & Worley, B., 1998. Calculating phase diagrams involving solid solutions via non-linear equations, with examples using THERMOCALC. *Journal of metamorphic Geology*, **16,** 577–588.

Rapela, C., Fanning, M., Baldo, E., Dahlquist, J., Pankhurst, R. & Murra, J., 2005. Coeval S- and I-type granites in the Sierra de Ancasti, Eastern Sierras Pampeanas, Argentina. *Gondwana Conference*, **12,** 307.

Rapela, C., Pankhurst, R., Casquet, C. *et al*., 2007. The Río de la Plata craton and the assembly of SW Gondwana. *Earth-Science Reviews*, **83,** 49–82.

Stüwe, K., 1997. Effective bulk composition changes due to cooling: a model predicting complexities in retrograde reaction textures. *Contributions to Mineralogy and Petrology*, **129,** 43–52.

Stüwe, K. & Powell, P., 1995. PT paths from modal proportions: application to the Koralm Complex, Eastern Alps. *Contributions to Mineralogy and Petrology*, **119,** 83–93.

Tinkham, D.K., Zuluaga, C.A. & Stowell, H.H., 2001. Metapelite phase equilibria modeling in MnNCKFMASH: the effect of variable Al_2O_3 and MgO/(MgO + FeO) on mineral stability. *Geological Materials Research*, **3,** 42.

Vernon, R.H., White, R.W. & Clarke, G.L., 2008. False metamorphic events inferred from misinterpretation of microstructural evidence and *P–T* data. *Journal of Metamorphic Geology*, **26,** 437–449.

White, R.W., Pomroy, N.E. & Powell, R., 2005. An in-situ metatexite-diatexite transition in upper amphibolite facies rocks from Broken Hill, Australia. *Journal of Metamorphic Geology*, **23,** 579–602.

Willner, A.P., 1983a. Evolución tectónica. In: *La geología de la Sierra de Ancasti* (eds Aceñolaza, F.G., Miller, H. & Toselli, A.), *Munster, Munstersche Forschungen zur Geologie und Paleontologie*, **59,** 157–187.

Willner, A.P., 1983b. Evolución metamórfica. In: *La geología de la Sierra de Ancasti* (eds. Aceñolaza, F.G., Miller, H. & Toselli, A.), *Munster, Munstersche Forschungen zur Geologie und Paleontologie*, **59,** 189–200.

Willner, A.P., Toselli, A.J., Basán, C. & Vides de Bazán, M.E., 1983. Rocas metamórficas. In: *La geología de la Sierra de Ancasti* (eds Aceñolaza, F.G., Miller, H. & Toselli, A.), *Munster, Munstersche Forschungen zur Geologie und Paleontologie*, **59,** 31–78.

Zeh, A., Millar, I.L. & Horstwood, A., 2004. Polymetamorphism in the NE Shackleton Range, Antarctica: constraints from Petrology and U-Pb, Sm-Nd, Rb-Sr TIMS and in situ U-Pb LA-PIMMS dating. *Journal of Petrology*, **45,** 949–973.

SUPPORTING INFORMATION

Additional Supporting Information may be found in the online version of this article at the publisher's web-site:

Table S1. Electron microprobe analyses of minerals from sample ANC-19000.

Please note: Wiley-Blackwell is not responsible for the content or functionality of any supporting materials supplied by the authors. Any queries (other than missing material) should be directed to the corresponding author for the article.

Received 11 October 2011; revision accepted 13 August 2012.